# nature materials

**Article** 

https://doi.org/10.1038/s41563-023-01690-2

# Thermally induced atomic reconstruction into fully commensurate structures of transition metal dichalcogenide layers

Received: 29 March 2023

Accepted: 13 September 2023

Published online: 12 October 2023



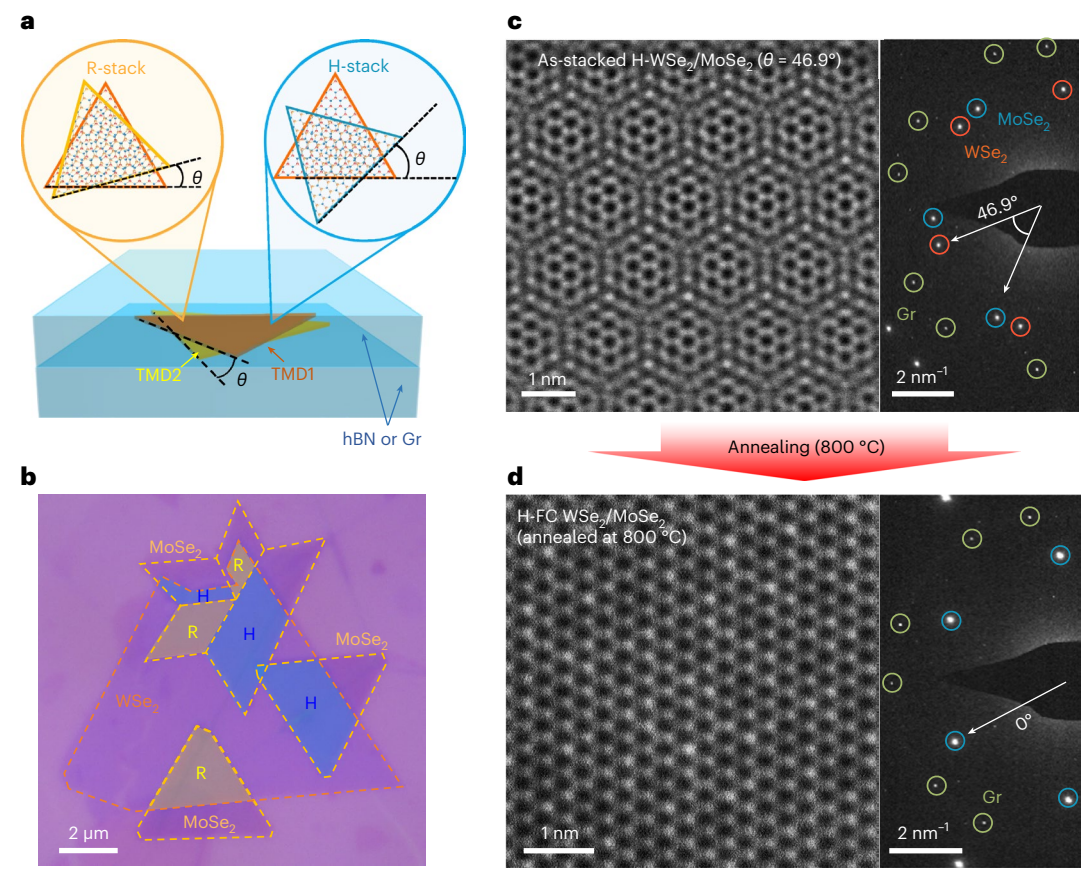
Ji-Hwan Baek <sup>1</sup>, Hyoung Gyun Kim¹, Soo Yeon Lim <sup>2</sup>, Seong Chul Hong <sup>1</sup>, Yunyeong Chang¹, Huije Ryu¹, Yeonjoon Jung¹, Hajung Jang², Jungcheol Kim², Yichao Zhang <sup>3</sup>, Kenji Watanabe <sup>4</sup>, Takashi Taniguchi <sup>5</sup>, Pinshane Y. Huang <sup>3</sup>, Hyeonsik Cheong <sup>2</sup>, Miyoung Kim¹ & Gwan-Hyoung Lee <sup>1</sup> □

Twist angle between two-dimensional layers is a critical parameter that determines their interfacial properties, such as moiré excitons and interfacial ferro-electricity. To achieve better control over these properties for fundamental studies and various applications, considerable efforts have been made to manipulate twist angle. However, due to mechanical limitations and the inevitable formation of incommensurate regions, there remains a challenge in attaining perfect alignment of crystalline orientation. Here we report a thermally induced atomic reconstruction of randomly stacked transition metal dichalcogenide multilayers into fully commensurate heterostructures with zero twist angle by encapsulation annealing, regardless of twist angles of as-stacked samples and lattice mismatches. We also demonstrate the selective formation of R- and H-type fully commensurate phases with a seamless lateral junction using chemical vapour-deposited transition metal dichalcogenides. The resulting fully commensurate phases exhibit strong photoluminescence enhancement of the interlayer excitons, even at room temperature, due to their commensurate structure with aligned momentum coordinates. Our work not only demonstrates a way to fabricate zero-twisted, two-dimensional bilayers with R- and H-type configurations, but also provides a platform for studying their unexplored properties.

Van der Waals (vdW) heterostructures of two-dimensional (2D) layers have been widely studied owing to their unprecedented physical properties, including superconductivity and Mott insulating phase in magic-angle graphene bilayer and moiré interlayer excitons and quantum mechanically hybridized electronic states in twisted transition metal dichalcogenide (TMD) bilayers<sup>1-9</sup>. Therefore, the twist

angle of two stacked layers has been considered a critical parameter in determination of the electronic and optical properties of twisted vdW heterostructures<sup>10–13</sup>. However, recent reports indicate that twisted bilayers undergo unconventional atomic reconstruction to relieve strain<sup>14–19</sup>, with stacked bilayers of large twist angle forming moiré superlattice structures due to the high energy required for atomic

<sup>1</sup>Department of Material Science and Engineering, Seoul National University, Seoul, Korea. <sup>2</sup>Department of Physics, Sogang University, Seoul, Korea. <sup>3</sup>Department of Materials Science and Engineering, University of Illinois at Urbana-Champaign, Urbana-Champaign, IL, USA. <sup>4</sup>Research Center for Electronic and Optical Materials, National Institute for Materials Science, Tsukuba, Japan. <sup>5</sup>Research Center for Materials Nanoarchitectonics, National Institute for Materials Science, Tsukuba, Japan. <sup>6</sup>Research Center for Materials Nanoarchitectonics, National Institute for Materials Science, Tsukuba, Japan. <sup>6</sup>Research Center for Materials Nanoarchitectonics, National Institute for Materials Science, Tsukuba, Japan. <sup>6</sup>Research Center for Materials Nanoarchitectonics, National Institute for Materials Science, Tsukuba, Japan. <sup>6</sup>Research Center for Materials Nanoarchitectonics, National Institute for Materials Science, Tsukuba, Japan. <sup>6</sup>Research Center for Materials Nanoarchitectonics, National Institute for Materials Science, Tsukuba, Japan. <sup>6</sup>Research Center for Materials Nanoarchitectonics, National Institute for Materials National Institute for Materials Nanoarchitectonics, National Institute for Materials National Institute for Materials National Institute for Materials National In



 $\label{lem:fig.1} \textbf{Fig. 1} | Atomic reconstruction to fully commensurate structure in twisted TMD vdW heterostructures. \textbf{a}, Schematic images of twisted TMD bilayers encapsulated by graphene (Gr) or hBN with a different stacking type (R- and H-stack). \textbf{b}, Optical image of Gr/WSe <math>_2$ /MoSe  $_2$ /Gr heterostructures with a different

stacking type. False-coloured regions indicate R-stack (yellow) and H-stack (blue) WSe $_2$ /MoSe $_2$  heterobilayers.  $\mathbf{c}$ ,  $\mathbf{d}$ , High-magnification HAADF–STEM images (left) and SAED images (right) of H-stack WSe $_2$ /MoSe $_2$  heterobilayers ( $\theta$  = 46.9°) asstacked ( $\mathbf{c}$ ) and following annealing ( $\mathbf{d}$ ).

reconstruction  $^{15,20}$ , and nearly-zero-stacked bilayers transforming into periodic commensurate domains separated by incommensurate (IC) boundaries with renormalized electronic band structures  $^{14,21}$ . Although zero-twisted bilayers are energetically stable in theory, the challenge lies in achieving perfect alignment of stacked 2D layers due to the inaccuracy of mechanical manipulators and the inevitable formation of IC boundaries as a result of spontaneous reconstruction.

Here we present a method for achieving fully commensurate (FC) heterostructures with zero twist angle by thermally induced atomic reconstruction of twisted 2D layers using encapsulation annealing regardless of the twist angles of as-stacked and lattice mismatches, resulting in perfectly aligned crystalline orientations of H- or R-type over entire stacked areas and opposite strains in adjacent layers. The FC heterostructure of two TMDs shows strong photoluminescence (PL) enhancement of interlayer excitons, reaching a thermal limit due to aligned electronic band edges in momentum space. We also demonstrate selective formation of R- and H-type FC phases with a seamless lateral junction by stacking 2D layers with parallel or antiparallel alignment of two constituent TMD layers.

# **Encapsulation annealing of twisted TMD layers**

To prevent decomposition of TMD layers and to provide encapsulation-induced pressure during annealing  $^{22-25}$ , we fabricated twisted TMD heterobilayers encapsulated by graphene or hexagonal boron nitride (hBN), as illustrated in Fig. 1a. The MX<sub>2</sub> (M = W, Mo and X = S, Se) was synthesized into triangular grains by chemical vapour deposition (CVD), which allows determination of the stacking types of TMD bilayers by aligning two grains: R-stack for parallel alignment and H-stack

for antiparallel alignment (see Methods for synthesis of TMDs and Supplementary Figs. 1 and 2 for alignment of stacked layers). Figure 1b shows the optical microscopic image of R- and H-stacks of WSe<sub>2</sub>/MoSe<sub>2</sub> by alignment of the triangular edges of TMD monolayers. As shown in the high-angle, annular dark-field scanning transmission electron microscopy (HAADF-STEM) image in Fig. 1c, moiré superlattices were observed in the as-stacked H-WSe<sub>2</sub>/MoSe<sub>2</sub> with a twist angle of 46.9° (measured using selected area electron diffraction (SAED) patterns). Note that we used graphene for encapsulation rather than hBN to obtain clear transmission electron microscopy (TEM) images. However, following encapsulation annealing at 800 °C for 3 h, the twisted bilayers were converted to an H-type FC (H-FC) heterostructure that has a 2H configuration (Fig. 1d). The SAED patterns of H-FC heterostructure in Fig. 1d indicate that crystalline orientations of WSe<sub>2</sub> and MoSe<sub>2</sub> were perfectly aligned following annealing. We also confirmed that R-stack WSe<sub>2</sub>/MoSe<sub>2</sub> was changed to R-type FC (R-FC) with atomic configuration of 3R following encapsulation annealing (Supplementary Fig. 3). It was reported that even the heterobilayer with zero twist angle has moiré superlattices owing to lattice mismatch between two TMDs<sup>12</sup>. However, we confirmed the absence of both angle and lattice mismatch in FC heterostructures by analysis of SAED patterns (Supplementary Fig. 4). Atomic reconstruction was not observed in non-encapsulated WSe<sub>2</sub>/ MoSe<sub>2</sub> following annealing under a Se-rich environment (Supplementary Fig. 5). Thus, encapsulation with graphene or hBN is essential for atomic reconstruction because vertical compression can be induced by encapsulation<sup>22,23</sup>. Furthermore, we also verified that similar atomic reconstruction occurs even in randomly stacked multilayers (up to four layers) of WSe<sub>2</sub> and MoS<sub>2</sub> with different twist angles at individual

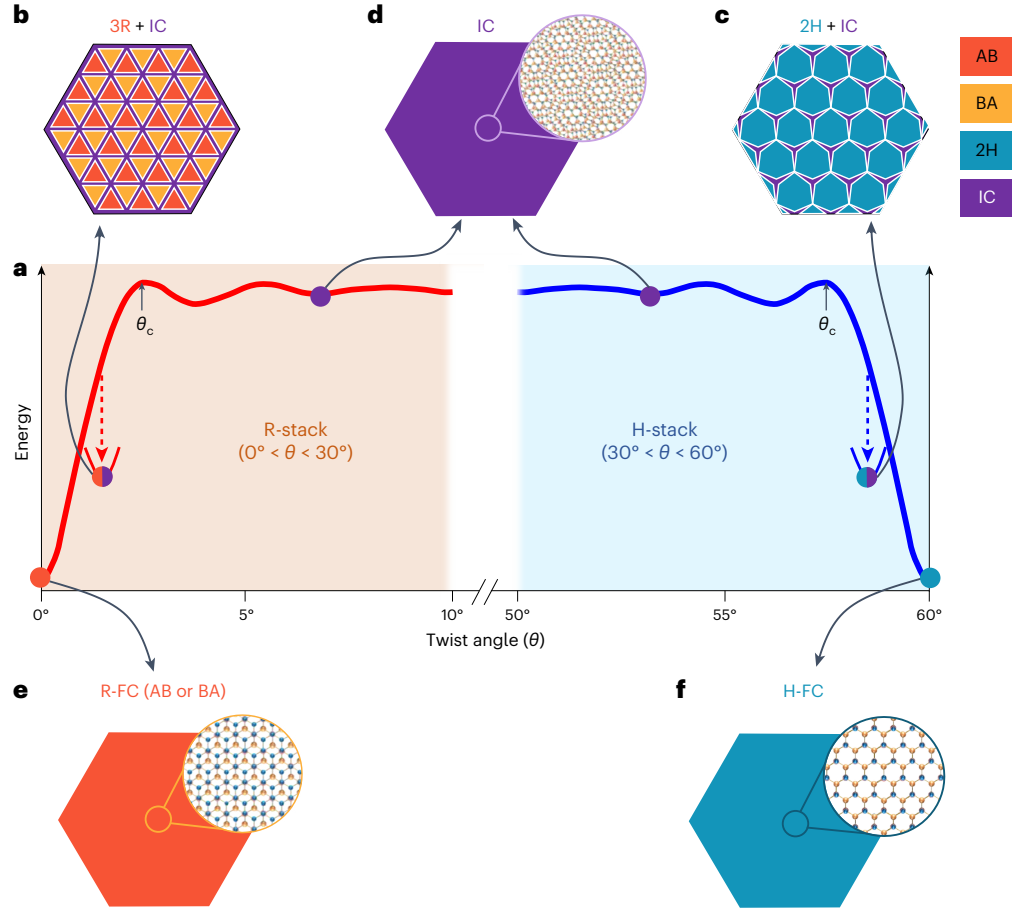


Fig. 2 | Dependence of stacking type and twist angle on thermally induced atomic reconstruction. a, Schematics of total vdW energy of twisted TMD bilayers as a function of twist angle.  $\mathbf{b}$ - $\mathbf{f}$ , Schematic illustrations of atomic structure of twisted TMDs by their stacking type and twist angle before  $(\mathbf{b}$ - $\mathbf{d})$  and

after (**e**, **f**) annealing. **b**, 3R + IC; **c**, 2H + IC; **d**, IC; **e**, R-FC; **f**, H-FC. Orange, yellow, blue and purple domains represent AB (3R), BA (3R), 2H and IC, respectively. Red, orange and blue circles represent W, Mo and Se atoms, respectively.

hetero-interfaces (Supplementary Figs. 6–8). Although we separately stacked four monolayers into twisted tetralayers, the entire stack transformed into FC phase following encapsulation annealing. The stacked layers show different critical temperatures for atomic reconstruction, depending on the types and combinations of TMDs; this is discussed below. We observed no change in heterobilayers of MoS $_2$ /MoSe $_2$  and WS $_2$ /WSe $_2$  with large lattice mismatches of -4% following annealing at up to 1,000 °C. This indicates that atomic reconstruction occurs only in the heterobilayer with a small lattice mismatch.

Figure 2 provides an overview of how the atomic reconstruction process of twisted TMD bilayers varies depending on stacking sequence and twist angle. The total vdW energy of twisted TMD bilayers calculated in ref. 26 is plotted as a function of twist angle for R- (red line) and H-stack (blue line) bilayers to show the twist-angle-dependent stability of moiré heterostructure and reconstructed phases (Fig. 2a)<sup>26</sup>. If the twist angle of R- and H-stack bilayers is less than critical angle  $(\theta_c)$ , which is almost zero, the stacked bilayers shows spontaneous atomic reconstruction into periodic domains of AB, BA or 2H separated by IC boundaries, as illustrated in Fig. 2b,c, without any external stimuli to minimize total vdW energy, as indicated by dashed arrows in Fig. 2a. The atomic structure of reconstructed domains depends on the stacking sequence, with the R-stack being 3R configuration and H-stack 2H configuration. Meanwhile, if the twist angle is higher than  $\theta_c$ , the twisted TMD bilayers maintain incommensurate moiré superlattices because of insufficient thermal energy at room temperature to overcome the energy barrier for spontaneous atomic reconstruction (Fig. 2d). Nevertheless, encapsulation annealing of twisted TMD bilayers over critical temperature results in atomic reconstruction into the FC structures shown in Fig. 2e,f, regardless of twist angle and stacking type. The atomic structure of FC bilayers is determined by their stacking type: R(H)-stack transforms into R(H)-FC, which has a 3R(2H) atomic configuration.

#### Structural characteristics of FC heterostructures

The HAADF-STEM image in Fig. 3a shows the partially overlapped region of H-stack WSe<sub>2</sub>/MoSe<sub>2</sub> bilayers with a twist angle of 29.5° following encapsulation annealing at 800 °C. The H-FC WSe<sub>2</sub>/MoSe<sub>2</sub> and its adjacent 1L-MoSe<sub>2</sub> area have identical crystal orientation while the distant monolayer MoSe<sub>2</sub> area retains its original crystal direction as indicated by zig-zag directions, resulting in a sharp boundary between two monolayer regions as indicated by the blue dashed line. The difference in crystalline orientations between reconstructed and pristine regions in 1L-MoSe<sub>2</sub> is 29.5°, which corresponds to the twist angle of the as-stacked WSe<sub>2</sub>/MoSe<sub>2</sub> bilayer. The magnified TEM image in Fig. 3b (red box in Fig. 3a) indicates that the nanometre-wide boundary has a highly distorted lattice structure with a few vacancies, which provides a barrier for propagation of atomic reconstruction. As shown in Fig. 3c, a few hexagonal areas of monolayer WSe<sub>2</sub> with aligned crystalline orientation are observed in the H-FC WSe<sub>2</sub>/MoSe<sub>2</sub> region. It is estimated that a MoSe<sub>2</sub> layer with either lower bond strength or higher defect density forms the nanoscale holes to relax the strain induced by atomic reconstruction, as reported for an annealed monolayer<sup>27</sup>.

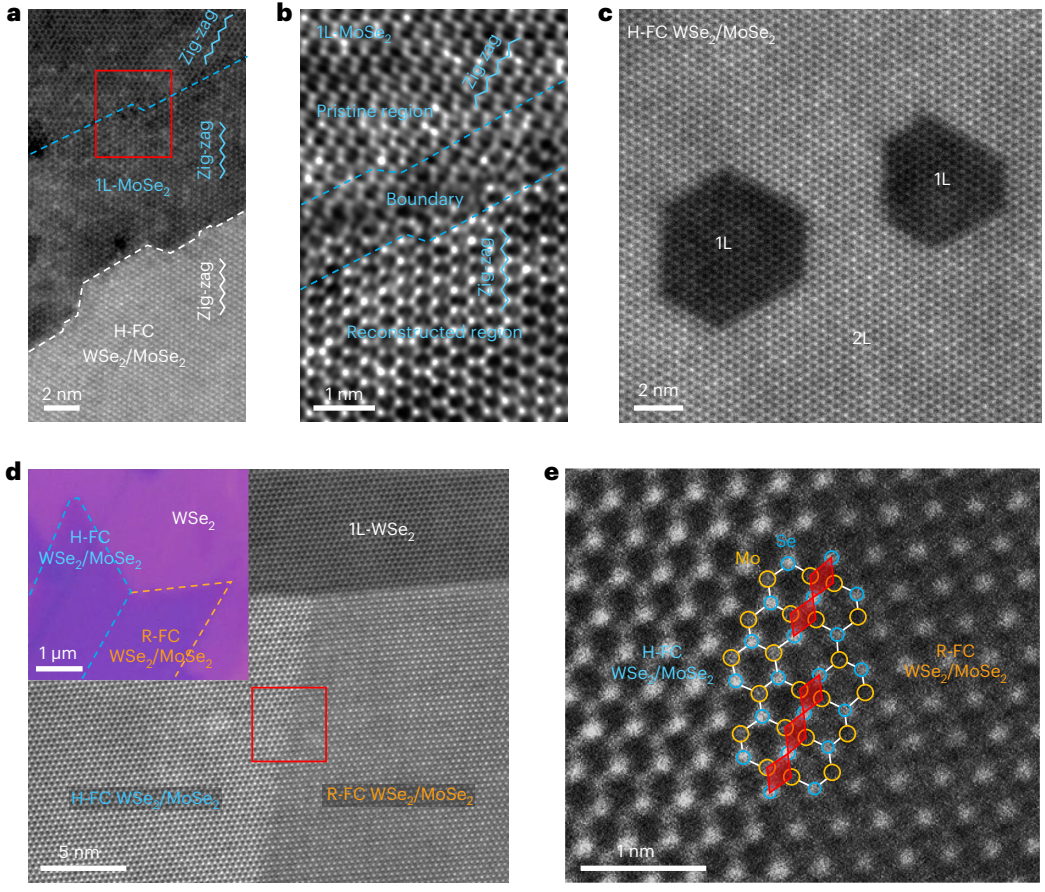


**Fig. 3** | **Structural characteristics of FC heterostructures. a,b**, HAADF–STEM images of partially overlapped regions of WSe $_2$ /MoSe $_2$ ( $\theta$  = 29.5°) following annealing. **c**, HAADF–STEM image of hexagonal regions of 1L-TMD in H-FC WSe $_2$ /MoSe $_2$  following annealing. **d**, HAADF–STEM image of partially overlapped

regions of single-crystal WSe $_2$  and polycrystalline MoSe $_2$ . Inset shows optical images of twisted WSe $_2$ /MoSe $_2$ . **e**, Magnified HAADF–STEM image of redbordered box in **d**. Circles represent Mo (orange) and Se (blue) atoms, and red rhombuses represent mirror twin boundaries of MoSe $_2$ .

To verify the stability of grain boundary during atomic reconstruction, we fabricated WSe<sub>2</sub>/MoSe<sub>2</sub> bilayers with grain boundaries between H- and R-stack regions using CVD-grown polycrystalline MoSe<sub>2</sub> and single-crystal WSe<sub>2</sub> (Supplementary Fig. 1). We transferred a star-shaped polycrystalline MoSe<sub>2</sub>, consisting of several grains with opposite crystalline orientations<sup>28-30</sup>, onto a single crystal of WSe<sub>2</sub> (Inset of Fig. 3d). Following encapsulation annealing, R- and H-FC heterostructures were formed, maintaining a seamless mirror twin boundary (Fig. 3e). This result is in agreement with migration of the mirror twin boundary with no damage to the atomic structure<sup>31</sup>. The nanoscale boundaries of Fig. 3b are present only in the monolayer MoSe<sub>2</sub> region while there is no such boundary in the monolayer WSe<sub>2</sub>, as shown in Fig. 3d. Our observations indicate that thermally induced atomic reconstruction in the stacked bilayers occurs via rearrangement of atoms in a weakly bonded layer, rather than by rotation of entire flakes. These agree well with the premise that MoSe<sub>2</sub> has weaker atomic bonding strength than WSe<sub>2</sub> and that TMDs with stronger atomic binding energy require higher temperatures for atomic reconstruction<sup>32</sup>. However, there is no clear preference in regard to whether the bottom or top layer undergoes atomic reconstruction in the case of homobilayers (Supplementary Fig. 9).

# Momentum-matched interlayer excitons in FC heterostructures

As shown in Fig. 4, we investigated the excitonic features of H-FC WSe<sub>2</sub>/MoSe<sub>2</sub> before and after encapsulation annealing by measurement of PL spectra at room temperature. Unlike randomly stacked

TMD bilayers<sup>33</sup>, H-FC WSe<sub>2</sub>/MoSe<sub>2</sub> showed significantly enhanced PL emission of interlayer excitons (X<sub>1</sub>) following annealing (Fig. 4a). The momentum mismatch of the first Brillouin zone (BZ) in the twisted TMD layers prohibits radiative recombination of interlayer excitons by the optical selection rule, as shown at the top of Fig. 4b (ref. 3). Meanwhile, the FC bilayers fabricated in this work facilitate the radiative recombination of interlayer excitons owing to alignment of the first BZ in momentum space (bottom of Fig. 4b). We also measured the PL spectra of randomly stacked WSe<sub>2</sub>/MoSe<sub>2</sub> by increasing the annealing temperature from 400 to 1,000 °C (Supplementary Fig. 10). The PL peak of interlayer excitons emerged following annealing at 800 °C, which is comparable to the temperature at which atomic reconstruction occurs (Fig. 1c,d). Although the shape of WSe<sub>2</sub> and MoSe<sub>2</sub> flakes did not change following annealing, PL peaks of interlayer excitons were strongly enhanced (Supplementary Fig. 11). Uniform PL intensities of interlayer excitons in H-FC WSe<sub>2</sub>/MoSe<sub>2</sub> also indicate the homogeneity of atomic reconstruction (Supplementary Fig. 12). We also used dark-field TEM to verify that the entire stacked region had the same orientation following encapsulation annealing (Supplementary Fig. 13). In the case of the R-stack WSe<sub>2</sub>/MoSe<sub>2</sub>, the enhanced PL peak of interlayer excitons exhibited lower energy due to the interlayer potential induced by intrinsic electric polarization of the 3R structure (Supplementary Figs. 14 and 15), which agrees with previous results<sup>34,35</sup>. The PL peaks of intralayer excitons for MoSe<sub>2</sub> (X<sub>M</sub>) and WSe<sub>2</sub> (X<sub>W</sub>) in H-WSe<sub>2</sub>/MoSe<sub>2</sub> exhibited blue and red shifts, respectively, following encapsulation annealing (Fig. 4c). The statistical measurements of PL shifts shown in Fig. 4d (measured from five samples) clearly show the opposite shifts

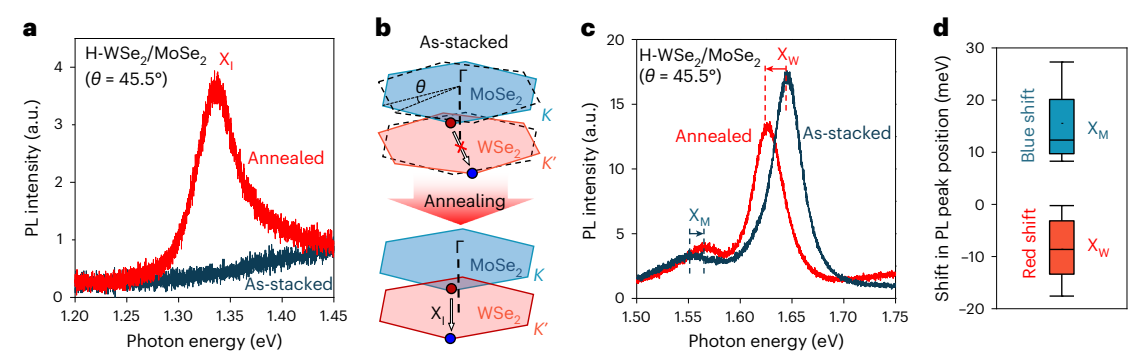


**Fig. 4** | **PL** measurements of hBN-encapsulated H-WSe<sub>2</sub>/MoSe<sub>2</sub> at room temperature. **a**, Interlayer exciton PL spectra of H-WSe<sub>2</sub>/MoSe<sub>2</sub> ( $\theta$  = 45.5°) before and after annealing. **b**, Schematic images of the first BZ of H-WSe<sub>2</sub>/MoSe<sub>2</sub> before and after annealing. *K* and *K'* indicate corners of first BZ of TMDs. Circles represent electrons (red) and holes (blue). **c**, Intralayer exciton PL spectra of

 $H-WSe_2/MoSe_2(\theta=45.5^\circ)\ before and after annealing.\ \textbf{d}, Shift in PL peak position of intralayer exciton of MoSe_2(X_M) and WSe_2(X_W) via encapsulation annealing. Data were obtained from five different samples. The median is represented by the centre lines in boxes, the boxes contain 25–75th percentiles of the dataset and whiskers represent minimum and maximum values. a.u., arbitrary units.$ 

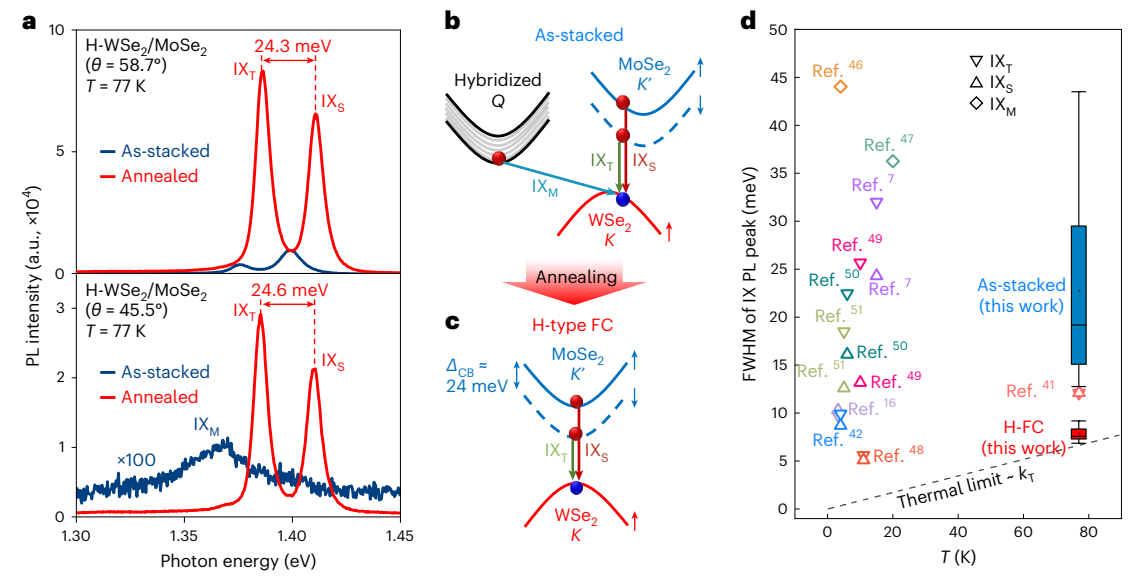


**Fig. 5** | **PL** measurements of hBN-encapsulated H-WSe $_2$ /MoSe $_2$  at 77 K. a, PL spectra of H-stack WSe $_2$ /MoSe $_2$  with  $\theta$  = 58.7 and 45.5° before and after annealing, respectively. IX $_{\rm M}$  denotes broad interlayer exciton (IX) PL peaks, and IX $_{\rm T}$  and IX $_{\rm S}$  indicate spin-singlet and spin-triplet interlayer excitons, respectively. **b,c**, Schematic images of the band structure at K and Q valley of as-stacked (**b**) and H-type FC (**c**) WSe $_2$ /MoSe $_2$  heterobilayers. Circles represent electrons (red) and

holes (jade). Solid and dashed lines represent spin-up and spin-down bands, respectively.  $\mathbf{d}$ , Full-width at half-maximum (FWHM) of PL peaks of IXs in H-stack WSe $_2$ /MoSe $_2$ . The data for H-FC in this work were obtained from six different samples. The median is represented by the centre lines in boxes, the boxes contain 25–75th percentiles of the dataset and whiskers represents minimum and maximum values.

of  $X_M$  and  $X_W$ . Moreover, the Raman spectra of H-WSe $_2$ /MoSe $_2$  show that the  $A_{1g}$  peak of MoSe $_2$  blue shifts while the A' and E' peaks of WSe $_2$  red shift following encapsulation annealing (Supplementary Fig. 16). This indicates that compressive and tensile strains are applied to MoSe $_2$  and WSe $_2$ , respectively  $^{36,37}$ . Therefore, PL shifts of  $(X_M)$  and WSe $_2(X_W)$  in the FC sample correspond to the opposite strains applied to constituent layers generated by formation of the FC heterostructure.

For precise probing of the energy states of interlayer excitons we measured the low-temperature PL spectra of two H-WSe $_2$ /MoSe $_2$  samples with twist angles of 58.7 and 45.5° at a temperature (T) of 77 K before and after encapsulation annealing. The as-stacked samples showed different PL features depending on their twist angle: small PL peaks of spin-singlet interlayer excitons (IX $_8$ ) and spin-triplet interlayer excitons (IX $_8$ ) for 58.7° and broad morie excitons (IX $_8$ ) for 45.5°, which has been reported elsewhere 4.6.7.16.38-40. In contrast, two H-FC samples fabricated by encapsulation annealing showed almost identical PL features with strongly enhanced PL intensities despite the different

twist angles: two distinct peaks of IX<sub>S</sub> and IX<sub>T</sub> due to large splitting of conduction band minimum (CBM) in MoSe<sub>2</sub> by strong spin-orbit coupling. The measured PL peak position differences between IX<sub>s</sub> and IX<sub>T</sub> (24.3-24.6 meV) shown in Fig. 5a are comparable to the energy difference between the up- and down-spin states of MoSe<sub>2</sub> ( $\Delta_{CR}$ )<sup>40,41</sup>. In the twisted heterobilayers of TMD, the valence band maximum (VBM) of WSe<sub>2</sub> and the CBM of MoSe<sub>2</sub> are displaced in the momentum space. The long-range symmetry of moiré superlattices generates a periodic potential that leads to band renormalization by interlayer hybridization of the wavefunctions of two TMDs, as depicted in Fig. 5b (refs. 7-9,12,36). Therefore, IX<sub>M</sub> (interlayer excitons trapped in the moiré potential) showed twist-angle-dependent PL characteristics in the twisted heterobilayers<sup>3</sup>. However, all H-FC heterobilayers fabricated in this work have the identical electronic band structure: the VBM of WSe<sub>2</sub> and CBM of MoSe<sub>2</sub> are aligned at the K valley in momentum space as shown in Fig. 5c, leading to similar PL characteristics of distinct IX<sub>s</sub> and IX<sub>T</sub>. Due to the absence of mirror symmetry in the

out-of-plane direction of heterobilayers,  $IX_T$  can contribute to radiative recombination in the heterobilayers, unlike in monolayer TMDs where  $IX_T$  are optically  $dark^{41,42}$ . As indicated by the blue box in Fig. 5d, the twisted heterobilayers show broad PL peaks of interlayer excitons owing to inhomogeneous moiré potential trap and random distribution of incommensurate domains in near-zero-stacked WSe<sub>2</sub>/MoSe<sub>2</sub> (refs. 43–45). Following encapsulation annealing we achieved much lower full-width at half-maximum values of  $IX_S$  and  $IX_T$  (-7.84 meV, indicated by the red box in Fig. 5d) in H-FC heterobilayers than those in other reports  $^{7,16,41,42,46-51}$ , reaching a thermal limit ( $k_T$  = -6.64 meV at 77 K) (Fig. 5d and Supplementary Fig. 17). The low full-width at half-maximum value of  $IX_S$  and  $IX_T$  PL peaks at low temperature also supports the structural homogeneity of FC structures (Supplementary Fig. 18).

The strong and narrow PL peaks of interlayer excitons close to theoretical values thus indicate the formation of uniform FC heterostructures with precise zero twist angles.

#### Conclusion

In this study we demonstrate an approach for achieving FC structures with zero twist angle and zero lattice mismatch by encapsulation annealing of randomly stacked TMD layers. Our method facilitated the selective formation of R- and H-type FC structures that can be easily obtained without epitaxial growth. Due to their commensurate structure with aligned momentum coordinates, the FC heterostructures show strong PL enhancement of interlayer excitons. These results not only provide a way to fabricate zero-twisted 2D bilayers with R- and H-type configurations, but also offer a promising platform for investigating the unexplored properties of vdW heterostructures such as interlayer excitons, interlayer valleys and interlayer ferro-electrics. In particular, R-FC is expected to be useful in research related to ferro-electricity or photovoltaic properties induced from an intrinsic electrical polarization in 3R-TMD homobilayers  $^{29,52-55}$ .

#### Online content

Any methods, additional references, Nature Portfolio reporting summaries, source data, extended data, supplementary information, acknowledgements, peer review information; details of author contributions and competing interests; and statements of data and code availability are available at https://doi.org/10.1038/s41563-023-01690-2.

#### References

- Cao, Y. et al. Unconventional superconductivity in magic-angle graphene superlattices. *Nature* 556, 43–50 (2018).
- Cao, Y. et al. Correlated insulator behaviour at half-filling in magic-angle graphene superlattices. Nature 556, 80–84 (2018).
- 3. Rivera, P. et al. Interlayer valley excitons in heterobilayers of transition metal dichalcogenides. *Nat. Nanotechnol.* **13**, 1004–1015 (2018).
- Yu, H., Liu, G.-B. & Yao, W. Brightened spin-triplet interlayer excitons and optical selection rules in van der Waals heterobilayers. 2D Mater. 5, 035021 (2018).
- Bai, Y. et al. Excitons in strain-induced one-dimensional moiré potentials at transition metal dichalcogenide heterojunctions. Nat. Mater. 19, 1068–1073 (2020).
- Shimazaki, Y. et al. Strongly correlated electrons and hybrid excitons in a moiré heterostructure. Nature 580, 472–477 (2020).
- 7. Tran, K. et al. Evidence for moiré excitons in van der Waals heterostructures. *Nature* **567**, 71–75 (2019).
- Jin, C. et al. Observation of moiré excitons in WSe<sub>2</sub>/WS<sub>2</sub> heterostructure superlattices. Nature 567, 76–80 (2019).
- Seyler, K. L. et al. Signatures of moiré-trapped valley excitons in MoSe<sub>2</sub>/WSe<sub>2</sub> heterobilayers. Nature 567, 66–70 (2019).
- Carr, S. et al. Twistronics: manipulating the electronic properties of two-dimensional layered structures through their twist angle. *Phys. Rev. B* 95, 075420 (2017).

- Liao, M. et al. Precise control of the interlayer twist angle in large scale MoS<sub>2</sub> homostructures. Nat. Commun. 11. 2153 (2020).
- Yuan, L. et al. Twist-angle-dependent interlayer exciton diffusion in WS<sub>2</sub>-WSe<sub>2</sub> heterobilayers. Nat. Mater. 19, 617–623 (2020).
- Liao, M. et al. Twist angle-dependent conductivities across MoS<sub>2</sub>/ graphene heterojunctions. Nat. Commun. 9, 4068 (2018).
- Yoo, H. et al. Atomic and electronic reconstruction at the van der Waals interface in twisted bilayer graphene. *Nat. Mater.* 18, 448–453 (2019).
- Weston, A. et al. Atomic reconstruction in twisted bilayers of transition metal dichalcogenides. Nat. Nanotechnol. 15, 592–597 (2020).
- Zhao, S. et al. Excitons in mesoscopically reconstructed moiré heterostructures. Nat. Nanotechnol. 18, 572–579 (2023).
- 17. Yasuda, K., Wang, X., Watanabe, K., Taniguchi, T. & Jarillo-Herrero, P. Stacking-engineered ferroelectricity in bilayer boron nitride. *Science* **372**, 1458–1462 (2021).
- Holler, J. et al. Low-frequency Raman scattering in WSe<sub>2</sub>-MoSe<sub>2</sub> heterobilayers: evidence for atomic reconstruction. *Appl. Phys. Lett.* 117, 013104 (2020).
- Rosenberger, M. R. et al. Twist angle-dependent atomic reconstruction and moiré patterns in transition metal dichalcogenide heterostructures. ACS Nano 14, 4550–4558 (2020).
- Quan, J. et al. Phonon renormalization in reconstructed MoS<sub>2</sub> moiré superlattices. Nat. Mater. 20, 1100–1105 (2021).
- 21. Zhu, S. & Johnson, H. T. Moiré-templated strain patterning in transition-metal dichalcogenides and application in twisted bilayer MoS<sub>2</sub>. *Nanoscale* **10**, 20689–20701 (2018).
- 22. Vasu, K. S. et al. Van der Waals pressure and its effect on trapped interlayer molecules. *Nat. Commun.* **7**, 12168 (2016).
- Han, X. et al. Effects of hexagonal boron nitride encapsulation on the electronic structure of few-layer MoS<sub>2</sub>. J. Phys. Chem. C Nanometer Interfaces 123, 14797–14802 (2019).
- 24. Ryu, H. et al. Anomalous dimensionality-driven phase transition of  $MoTe_2$  in van der Waals heterostructure. *Adv. Funct. Mater.* **31**, 2107376 (2021).
- 25. Li, J., Jia, L., Zheng, X., Peng, C. & Fu, X. Structural and elastic properties of WSe<sub>2</sub>: first-principles calculations. *J. Phys. Conf. Ser.* **1634**, 012145 (2020).
- Zhu, S., Pochet, P. & Johnson, H. T. Controlling rotation of two-dimensional material flakes. ACS Nano 13, 6925–6931 (2019).
- Chen, J. et al. In situ high temperature atomic level dynamics of large inversion domain formations in monolayer MoS<sub>2</sub>. Nanoscale 11, 1901–1913 (2019).
- Liu, Z. et al. Strain and structure heterogeneity in MoS<sub>2</sub> atomic layers grown by chemical vapour deposition. *Nat. Commun.* 5, 5246 (2014).
- Zheng, W. et al. Controlled growth of six-point stars MoS<sub>2</sub> by chemical vapor deposition and its shape evolution mechanism. Nanotechnology 28, 395601 (2017).
- 30. van der Zande, A. M. et al. Grains and grain boundaries in highly crystalline monolayer molybdenum disulphide. *Nat. Mater.* **12**, 554–561 (2013).
- 31. Zhao, X. et al. Healing of planar defects in 2D materials via grain boundary sliding. *Adv. Mater.* **31**, e1900237 (2019).
- Singh, Y., Back, S. & Jung, Y. Activating transition metal dichalcogenides by substitutional nitrogen-doping for potential ORR electrocatalysts. *ChemElectroChem* 5, 4029–4035 (2018).
- 33. Nayak, P. K. et al. Probing evolution of twist-angle-dependent interlayer excitons in MoSe<sub>2</sub>/WSe<sub>2</sub> van der Waals heterostructures. *ACS Nano* **11**, 4041–4050 (2017).
- 34. Paradisanos, I. et al. Controlling interlayer excitons in MoS<sub>2</sub> layers grown by chemical vapor deposition. *Nat. Commun.* **11**, 2391 (2020).

- Yang, D. et al. Spontaneous-polarization-induced photovoltaic effect in rhombohedrally stacked MoS<sub>2</sub>. Nat. Photonics 16, 469–474 (2022).
- Dadgar, A. M. et al. Strain engineering and Raman spectroscopy of monolayer transition metal dichalcogenides. *Chem. Mater.* 30, 5148–5155 (2018).
- Horzum, S. et al. Phonon softening and direct to indirect band gap crossover in strained single-layer MoSe<sub>2</sub>. Phys. Rev. B 87, 125415 (2013).
- Tang, Y. et al. Tuning layer-hybridized moiré excitons by the quantum-confined Stark effect. Nat. Nanotechnol. 16, 52–57 (2021).
- Wang, L. et al. Correlated electronic phases in twisted bilayer transition metal dichalcogenides. *Nat. Mater.* 19, 861–866 (2020).
- Zhang, L. et al. Highly valley-polarized singlet and triplet interlayer excitons in van der Waals heterostructure. *Phys. Rev. B* 100, 041402 (2019).
- Wang, T. et al. Giant Valley-Zeeman splitting from spin-singlet and spin-triplet interlayer excitons in WSe<sub>2</sub>/MoSe<sub>2</sub> heterostructure. Nano Lett. 20, 694–700 (2020).
- 42. Li, Z. et al. Interlayer exciton transport in MoSe<sub>2</sub>/WSe<sub>2</sub> heterostructures. ACS Nano 15, 1539–1547 (2021).
- Schubert, E. F., Göbel, E. O., Horikoshi, Y., Ploog, K. & Queisser, H. J. Alloy broadening in photoluminescence spectra of Al<sub>x</sub>Ga<sub>1-x</sub>As. *Phys. Rev. B* 30, 813–820 (1984).
- 44. Cadiz, F. et al. Excitonic lidth approaching the homogeneous limit in MoS<sub>2</sub>-based van der Waals heterostructures. *Phys. Rev. X* 7, 021016 (2017).
- 45. Merritt, T. R. et al. Photoluminescence lineshape and dynamics of localized excitonic transitions in InAsP epitaxial layers. *J. Appl. Phys.* **115**, 193503 (2014).
- Hsu, W. T. et al. Negative circular polarization emissions from WSe<sub>2</sub>/MoSe<sub>2</sub> commensurate heterobilayers. *Nat. Commun.* 9, 1356 (2018).

- Rivera, P. et al. Observation of long-lived interlayer excitons in monolayer MoSe<sub>2</sub>-WSe<sub>2</sub> heterostructures. *Nat. Commun.* 6, 6242 (2015).
- Hanbicki, A. T. et al. Double indirect interlayer exciton in a MoSe<sub>2</sub>/ WSe<sub>2</sub> van der Waals heterostructure. ACS Nano 12, 4719–4726 (2018).
- 49. Alexeev, E. M. et al. Emergence of highly linearly polarized interlayer exciton emission in MoSe<sub>2</sub>/WSe<sub>2</sub> heterobilayers with transfer-niduced layer corrugation. ACS Nano 14, 11110–11119 (2020).
- 50. Wu, B. et al. Observation of double indirect interlayer exciton in MoSe<sub>2</sub>/WSe<sub>2</sub> heterostructure. *Nano Res.* **15**, 2661–2666 (2021).
- 51. Mahdikhanysarvejahany, F. et al. Temperature dependent moiré trapping of interlayer excitons in MoSe<sub>2</sub>-WSe<sub>2</sub> heterostructures. *NPJ 2D Mater. Appl.* **5**, 67 (2021).
- Ciarrocchi, A. et al. Polarization switching and electrical control of interlayer excitons in two-dimensional van der Waals heterostructures. *Nat. Photonics* 13, 131–136 (2019).
- Wang, X. et al. Interfacial ferroelectricity in rhombohedral-stacked bilayer transition metal dichalcogenides. *Nat. Nanotechnol.* 17, 367–371 (2022).
- 54. Deb, S. et al. Cumulative polarization in conductive interfacial ferroelectrics. *Nature* **612**, 465–469 (2022).
- Rogée, L. et al. Ferroelectricity in untwisted heterobilayers of transition metal dichalcogenides. Science 376, 973–978 (2022).

**Publisher's note** Springer Nature remains neutral with regard to jurisdictional claims in published maps and institutional affiliations.

Springer Nature or its licensor (e.g. a society or other partner) holds exclusive rights to this article under a publishing agreement with the author(s) or other rightsholder(s); author self-archiving of the accepted manuscript version of this article is solely governed by the terms of such publishing agreement and applicable law.

@ The Author(s), under exclusive licence to Springer Nature Limited 2023

## Methods

#### Chemical vapour deposition growth

Monolayer crystals of WSe, and MoSe, were synthesized on SiO<sub>2</sub>/Si substrates with SiO<sub>2</sub> thickness of 285 nm by CVD with a 2-inch guartz tube under ambient pressure. To synthesize monolayer WSe<sub>2</sub>, a quartz boat with WO<sub>2.9</sub> powder (99.99%, Alfa Aesar) and KI powder (99.99%, Alfa Aesar) was located in the centre of the furnace and the SiO<sub>2</sub>/Si substrate suspended face-down on top of the boat. Another quartz boat with selenium powder (99.99%, Sigma-Aldrich) was located upstream of the guartz tube at a distance of 19.5 cm from the centre of the furnace. The furnace temperature was raised to 800 °C at a rate of 50 °C min<sup>-1</sup> and maintained for 15 min, and then the furnace was naturally cooled to room temperature. Ar (300 standard cubic centimetres min<sup>-1</sup> (sccm) was flowed for the entire growth process and 10 sccm of H<sub>2</sub> flowed until the start of the cooling process. To synthesize monolayer MoSe<sub>2</sub>, a quartz boat with MoO<sub>3</sub> powder (99.97%, Sigma-Aldrich) was located in the centre of the furnace and the SiO<sub>2</sub>/Si substrate suspended face-down on top of the boat. Another quartz boat with selenium powder (99.99%, Sigma-Aldrich) was located upstream of the quartz tube at a distance of 19.5 cm from the centre of the furnace. The furnace temperature was raised to 750 °C at a rate of 50 °C min<sup>-1</sup> and maintained for 20 min, and then the furnace was naturally cooled to room temperature. Ar (300 sccm) was flowed for the entire growth process, and 10 sccm of H<sub>2</sub> was introduced from 20 to 35 min after the start of the growth process.

#### Sample preparation

Flakes of hBN-graphene were first mechanically exfoliated from bulk crystals onto silicon substrates with a 285-nm silicon oxide layer. Monolayer WSe<sub>2</sub> and MoSe<sub>2</sub> were either mechanically exfoliated from bulk crystals (from HQ Graphene) or synthesized from CVD. The thickness of monolayer WSe<sub>2</sub> and MoSe<sub>2</sub> was identified by optical contrast, PL measurements and atomic force microscopy. Next, hBN/WSe<sub>2</sub>/ MoSe<sub>2</sub>/hBN heterostructures for PL measurement were assembled with polycarbonate/polydimethylsiloxane using a dry-transfer method<sup>56</sup> with pick-up temperatures for hBN and TMDs at around 115 and 75 °C, respectively. Following stacking, heterostructures were transferred onto a clean SiO<sub>2</sub>/Si substrate by release of the polycarbonate film from the polydimethylsiloxane lens at >180 °C. Finally, transferred samples were placed in chloroform for 3 h to remove the polycarbonate film covering heterostructures. Similarly to hBN-encapsulated TMD bilayers, graphene-encapsulated TMD bilayers for TEM and STEM imaging were fabricated by the dry-transfer method. To prevent degradation of heterostructures during annealing, bi- or trilayer graphene was used<sup>24</sup>. However, since it is difficult to detach graphene from the SiO<sub>2</sub>/ Si substrate due to the stronger adhesion force between Gr/SiO<sub>x</sub> rather than hBN/SiO<sub>x</sub> (ref. 57), hBN was used as a top layer for easy detachment of the graphene. Thus, hBN/Gr/TMDs/Gr heterostructures were fabricated initially. Next, a XeF<sub>2</sub> gas, which can selectively etch only hBN remaining on the graphene<sup>58</sup>, was treated on the heterostructures to remove the top hBN. To induce atomic reconstruction in the twisted TMD layers, encapsulated TMD layers were annealed at >800 °C for 3 h in a vacuum of 10<sup>-4</sup> Torr. Annealing temperature was varied according to the combination of constituent TMDs: 800 °C for WSe<sub>2</sub>/MoSe<sub>2</sub> and MoSe<sub>2</sub>/MoSe<sub>2</sub>, 900 °C for MoS<sub>2</sub>/MoS<sub>2</sub> and 950 °C for WSe<sub>2</sub>/WSe<sub>2</sub>. The raising time for furnace temperature was 1 h and the furnace was naturally cooled to room temperature.

#### TEM

Transmission electron microscopy samples were prepared using a poly(methyl methacrylate)-based wet-transfer method. Samples on poly(methyl methacrylate) film were transferred on  $\mathrm{Si}_3\mathrm{N}_4$  TEM grids (TEM windows, no. SN100-A20MP2Q05). The poly(methyl methacrylate) film was removed by placing samples in acetone for 24 h. HAADF–STEM images and SAED patterns were acquired using Cs-corrected monochromated TEM/STEM (Themis Z) at an operating

voltage of 80 kV and a probe current of 30 pA, a 25 -mrad convergence angle and a collection angle range of 84 -- 200 mrad.

#### Raman and PL spectroscopy

Low-frequency Raman spectra were acquired using Raman spectroscopy (Horiba LabRAM HR Evolution) with a 532-nm laser and a spot size of ~1  $\mu m$ . PL spectra were acquired using Raman spectroscopy (JASCO) with a 532-nm laser and a spot size of ~1  $\mu m$ . Micro-PL measurements at low temperature were conducted with a diode-pumped, solid-state laser with wavelength of 532 nm (2.33 eV) and power of ~100  $\mu W$ . We used a ×40 objective lens (numerical aperture 0.6) to focus the laser on the samples with a spot of diameter ~1  $\mu m$  and to collect PL signals from samples. A substrate with exfoliated samples was loaded into an optical cryostat (Oxford MicrostatHe2) and cooled to 10 K with liquid helium. PL signals from samples were dispersed with a Horiba TRIAX 320 spectrometer (300 grooves mm $^{-1}$ ) and were detected with a charge-coupled device using liquid nitrogen for cooling. Raman and PL spectra were obtained at the same position before and after annealing.

## **Data availability**

All data needed to evaluate the conclusions are presented in the article and the Supplementary Information. Source data are provided with this paper.

#### References

- Pizzocchero, F. et al. The hot pick-up technique for batch assembly of van der Waals heterostructures. *Nat. Commun.* 7, 11894 (2016).
- 57. Rokni, H. & Lu, W. Direct measurements of interfacial adhesion in 2D materials and van der Waals heterostructures in ambient air. *Nat. Commun.* **11**, 5607 (2020).
- Son, J. et al. Atomically precise graphene etch stops for three dimensional integrated systems from two dimensional material heterostructures. *Nat. Commun.* 9, 3988 (2018).

# Acknowledgements

This work was supported by National Research Foundation of Korea Grants funded by the Korean Government (nos. 2021R1A2C3014316, 2021M3F3A2A01037858 and 2017R1A5A1014862 (SRC programme: vdWMRC centre)) and the Creative-Pioneering Researchers Programme through Seoul National University, S.Y.L., H.J., J.K. and H.C. acknowledge the support by the National Research Foundation of Korea Grant funded by the Korean Government (no. 2019R1A2C3006189). K.W. and T.T. acknowledge the support from the Japan Society for the Promotion of Science, KAKENHI (grant nos. 19H05790, 20H00354 and 21H05233) and from A3 Foresight by the Japan Society for the Promotion of Science. Support for P.Y.H. was provided by the Illinois Materials Research Science and Engineering Center through the National Science Foundation MRSEC programme (award no. DMR-1720633). G.-H.L. acknowledges the support from the Research Institute of Advanced Materials, Institute of Engineering Research, Institute of Applied Physics and Inter-University Semiconductor Research Center at Seoul National University.

### **Author contributions**

J.-H.B. and G.-H.L. designed and conceived the project. H.G.K., Y.C. and M.K. performed TEM and HAADF–STEM imaging. S.Y.L., H.J., J.K. and H.C. performed PL measurements at low temperature. H.R. fabricated samples for PL measurement. S.C.H. and Y.J. synthesized TMDs by CVD. Y.Z. and PY.H. discussed TEM and STEM results. K.W. and T.T. supplied boron nitride crystals. J.-H.B. and G.-H.L. jointly analysed the data and wrote the paper.

#### **Competing interests**

The authors declare no competing interests.

# **Additional information**

**Supplementary information** The online version contains supplementary material available at https://doi.org/10.1038/s41563-023-01690-2.

 $\begin{tabular}{ll} \textbf{Correspondence and requests for materials} should be addressed to \\ \textbf{Gwan-Hyoung Lee}. \end{tabular}$ 

**Peer review information** *Nature Materials* thanks Wen-Hao Chang, Ziliang Ye and the other, anonymous, reviewer(s) for their contribution to the peer review of this work.

**Reprints and permissions information** is available at www.nature.com/reprints.